Supporting Information

Structure and Redox Behaviour of a Paramagnetic Rh–Pt–Cu–Pt–Rh Heterometallic-Extended Metal -Atom Chain

Kazuhiro Uemura,* Yuya Ikeda

Department of Chemistry and Biomolecular Science, Faculty of Engineering, Gifu University, Yanagido 1-1, Gifu, 501-1193, Japan

* Tel: (+81)-58-293-2561, Fax: (+81)-58-293-2561, E-mail: uemura.kazuhiro.x1@f.gifu-u.ac.jp

Materials.

K$_2$PtCl$_4$ and RhCl$_3$·3H$_2$O were obtained from Tanaka Kikinzoku Co. CuCl$_2$ and PPh$_3$ were obtained from Nacalai Tesque Co. NaPF$_6$ was obtained from Tokyo Chemical Industry Co. (Bu$_4$N)Cl was obtained from Wako Co. [PtRhCl$_3$(piam)$_2$(NH$_3$)$_2$]·4H$_2$O,[S1] [PtRhCl$_2$(piam)$_2$(NH$_3$)$_2$(PPh$_3$)]PF$_6$,[S2] and (Bu$_4$N)$_2$[CuCl$_4$][S3] were synthesized according to previous procedure.

Synthesis of [PtRhCl$_2$(piam)$_2$(NH$_3$)$_2$(PPh$_3$)]$_2$[CuCl$_4$]·2MeCN (2)

A MeCN solution (10 mL) containing [PtRhCl$_2$(piam)$_2$(NH$_3$)$_2$(PPh$_3$)]PF$_6$ (**1**, 91 mg, 90 μmol) was mixed with (Bu$_4$N)$_2$[CuCl$_4$] (21 mg, 30 μmol) and stirred for several minutes to afford pale orange. After removing the powder, resulted orange solution was slowly evaporated in the tube (diameter 10 mm) to obtain dark orange single crystals for [PtRhCl$_2$(piam)$_2$(NH$_3$)$_2$(PPh$_3$)]$_2$[CuCl$_4$]·2MeCN (**2**). (24 mg, 12 μmol). Yield was 26%. Elemental analysis calcd for C$_{60}$H$_{88}$Cl$_8$CuN$_{10}$O$_4$P$_2$Pt$_2$Rh$_2$: C, 35.70%; H, 4.39%; and N, 6.94%, found: C, 35.38%; H, 4.41%; and N, 6.95%.

Synthetic studies for isolation of [PtRhCl$_2$(piam)$_2$(NH$_3$)$_2$(PPh$_3$)]$_2$[CuCl$_4$]·2MeCN (2)

Single crystals of **2** and [PtRhCl$_2$(piam)$_2$(NH$_3$)$_2$(PPh$_3$)]$_2$[CuCl$_3$] (**3**) will not deposit unless the reaction solution is evaporated. The following experiments were performed to optimise the synthesis of **2** and **3**. According to the previous procedure,[S2] Cl$^-$ axially contacted [PtRhCl$_2$(piam)$_2$(NH$_3$)$_2$(PPh$_3$)]Cl was obtained via the slow evaporation of MeCN solution (3 mL) containing **1** (20 μmol) and (Bu$_4$N)Cl (40 μmol). Meanwhile, **3** was obtained via the slow evaporation

of the MeCN (3 mL) solution after removing the pale orange powder of [PtRhCl$_2$(piam)$_2$(NH$_3$)$_2$(PPh$_3$)]Cl from the initial solution (10 mL) containing **1** (90 μmol) and (Bu$_4$N)$_2$[CuCl$_4$] (30 μmol), and the solution volume (10 mL) was rapidly concentrated to 3 mL. Compound **1** tends to become [PtRhCl$_2$(piam)$_2$(NH$_3$)$_2$(PPh$_3$)]Cl when Cl$^-$ ions are present in the system. Even if **1** is mixed with (Bu$_4$N)$_2$[PtCl$_4$] or (Bu$_4$N)$_2$[PdCl$_4$], from which Cl$^-$ ions are difficult to release, [PtRhCl$_2$(piam)$_2$(NH$_3$)$_2$(PPh$_3$)]Cl does not appear, indicating that Cl$^-$ ions equatorially coordinated to copper, which is involved in the generation of [PtRhCl$_2$(piam)$_2$(NH$_3$)$_2$(PPh$_3$)]Cl. The slowl evaporation of orange MeCN suspension (3 mL) containing **1** (40 μmol) and (Bu$_4$N)$_2$[CuCl$_4$] (20 μmol), without removing [PtRhCl$_2$(piam)$_2$(NH$_3$)$_2$(PPh$_3$)]Cl from the initial solution, can form single crystals of compound **3**; however, additional red crystals for [PtRhCl$_2$(piam)$_2$(NH$_3$)$_2$(PPh$_3$)]$_2$[PtCl$_4$], which are one-dimensional pentanuclear complex aligned as Rh–Pt–Pt–Pt–Rh, appeared in large amounts of pale orange powder of [PtRhCl$_2$(piam)$_2$(NH$_3$)$_2$(PPh$_3$)]Cl, which indicate that released Cl$^-$ ions are involved in highly complex reactions.

We, then, compared the amount of deposited [PtRhCl$_2$(piam)$_2$(NH$_3$)$_2$(PPh$_3$)]Cl by changing the proportions of **1** and (Bu$_4$N)$_2$[CuCl$_4$]. Mixing **1** (20 μmol) and 0.25, 0.5, 1.0, or 2.0 equivalent (Bu$_4$N)$_2$[CuCl$_4$] in MeCN (3 mL) forms 1.4 μmol, 8.4 μmol, 14 μmol, and 11 μmol of pale orange powder for [PtRhCl$_2$(piam)$_2$(NH$_3$)$_2$(PPh$_3$)]Cl, all of which did not show the EPR signal. By contrast, EPR measurements for the MeCN solution (1 mL) containing **1** (0.5 μmol) and (Bu$_4$N)$_2$[CuCl$_4$] (0.13 μmol) after removing the precipitated [PtRhCl$_2$(piam)$_2$(NH$_3$)$_2$(PPh$_3$)]Cl showed the signal attributed to the d^9 species, indicating the presence of paramagnetic species in the solution.

Based on the above studies, we considered that the solution contained **1** and Cu^{II} in an approximate ratio of 2:1 when **1** and (Bu$_4$N)$_2$[CuCl$_4$] were mixed at a ratio of 3:1, and after removing the precipitated [PtRhCl$_2$(piam)$_2$(NH$_3$)$_2$(PPh$_3$)]Cl. As shown in Scheme S1, we investigated the conditions for depositing single crystals of **2** and **3**, where quantitative information on the retention of paramagnetism in the solution was obtained from EPR measurements. Mixing MeCN solution (A, 10 mL) containing (Bu$_4$N)$_2$[CuCl$_4$] (30 μmol) with **1** (90 μmol) formed [PtRhCl$_2$(piam)$_2$(NH$_3$)$_2$(PPh$_3$)]Cl (36.4 mg, 40 μmol) as pale orange precipitate (D). Upon removing the precipitate, the orange solution (B, 10 mL) was concentrated to 3 mL (C) and slowly evaporated to obtain **3** (5 mg, 2.6 mol, yield 9%) and single crystals of [PtRhCl$_2$(piam)$_2$(NH$_3$)$_2$(PPh$_3$)]Cl. On the other hand, following the removal of the precipitate, the orange solution (B, 10 mL) was slowly evaporated in a glass tube (10 mm internal diameter) over 2 weeks to afford **2** (24 mg, 12 μmol, yield 26%). Figure S1 shows the EPR spectra at 77 K for glasses A–C, for which area ratios were 1.00 (A), 0.51 (B), 0.42 (C), indicating that the paramagnetic species decreases as A > B > C. The paramagnetic

density of C is lower than that of B, probably because the concentration of the solution promotes redox between Cu^{II} and Pt–Rh complexes. Evaporation of concentrated solution in a narrow tube to prevent reoxidation, is thought to yield diamagnetic **3**. On the other hand, the paramagnetic **2** could have been obtained by evaporation without concentration, by exposing it to air in the vial and promoting reoxidation.

X-ray Structure Determination.

Measurements were carried out on a Rigaku Mercury CCD diffractometer equipped with a normal focus Mo-target X-ray tube ($\lambda = 0.71073$ Å), operated at 5 kW power (50 kV, 100 mA). The system was equipped with a CCD two-dimensional detector. A total of 744 frames were collected using a scan width of 0.5° and an exposure time of 2 s/frame. The system was operated with the CrysAlisPRO software package.[S4] Empirical absorption correction using spherical harmonics was implemented in SCALE3 ABSPACK scaling algorithm.[S5] The structure was solved by direct methods[S6] with subsequent difference Fourier synthesis and refinement using SHELX-2017[S7] controlled by the Yadokari-XG software package.[S8] Non-hydrogen atoms were refined anisotropically and all hydrogen atoms were treated as riding atoms. The crystal data and structure refinement results are summarized in Table S1. Deposition Number 2325966 contains the supplementary crystallographic data for this paper.

Physical Measurements.

Elemental analysis for carbon, hydrogen, and nitrogen was performed using a J-Science JM10. UV–vis spectra were recorded using a Shimadzu UV3100PC at room temperature. The infrared (IR) spectra were recorded on a JASCO FT/IR-4600AC spectrometer over the range of 400–4000 cm^{-1} at room temperature. X-ray photoelectron spectroscopy (XPS) measurements were carried out at room temperature using a Quantera SXM spectrometer. Binding energies were measured relative to the C 1s peak (284.8 eV) of an internal hydrocarbon. The diffuse reflectance spectra were recorded at room temperature on a JASCO V-770ST spectrometer over the range of 320–2500 nm. ESI-MS were measured on a JEOL Accu-TOF. EPR spectra were measured on a JEOL TE-200 spectrometer. Cyclic voltammetric measurements were conducted at room temperature using a BAS 617E electrochemical analyzer. Conventional three electrode arrangement consisting of a glassy carbon working electrode, SCE reference electrode, and Pt wire counter electrode was used.

Density Functional Theory Calculation.

The electronic structure of the [{PtRhCl$_2$(NHCOCH$_3$)$_2$(NH$_3$)$_2$(PMe$_3$)}$_2${CuCl$_4$}] model compound was determined using the density functional theory (DFT) method and the Beck 3-parameter Lee–Yang–Parr (B3LYP) function[S9] with the Gaussian 16 program package.[S10] For platinum and rhodium, the LANL2DZ basis set was used with the Hay–Wadt effective core potential.[S11] For the other elements, 6–31G** basis sets[S12] were selected. The geometrical parameters obtained from the crystal structure data of **2** were used to prepare the initial models for optimization. For the models, full geometry optimization was conducted under frozen conditions for metals and coordination atoms considering solvent effect, and 80 excited states were obtained on the basis of the structure to determine vertical excitation energy using Td-DFT calculations.[S13, S14]

Supplementary References

S1.   K. Uemura, K. Yamasaki, K. Fukui and K. Matsumoto, *Eur. J. Inorg. Chem.*, 2007, 809–815.
S2.   K. Uemura, Y. Ikeda, A. Takamori, T. Takeyama and S. Iwatsuki, *Chem. Eur. J.*, 2023, **29**, e202204057.
S3.   A. Winter, A. Zabel and P. Strauch, *Int. J. Mol. Sci.*, 2012, **13**, 1612–1619.
S4.   CrysAlisPRO, Oxford Diffraction /Agilent Technologies UK Ltd, Yarnton, England.
S5.   SCALE3 ABSPACK, An Oxford Diffraction program, Oxford Diffraction Ltd, 2005.
S6.   A. Altomare, M. C. Burla, M. Camalli, G. L. Cascarano, C. Giacovazzo, A. Guagliardi, A. G. G. Moliterni, G. Polidori and R. Spagna, *J. Appl. Crystallogr.*, 1999, **32**, 115–119.
S7.   G. M. Sheldrick, *Acta Crystallogr.*, 2008, **A64**, 112–122.
S8.   C. Kabuto, S. Akine, T. Nemoto, E. Kwon, *J. Crystallogr. Soc. Jpn.* **2009**, *51*, 218–224.
S9.   a) C. T. Lee, W. T. Yang, R. G. Parr, *Phys. Rev. B* **1988**, *37*, 785–789; b) B. Miehlich, A. Savin, H. Stoll, H. Preuss, *Chem. Phys. Lett.* **1989**, *157*, 200–206; c) A. D. Becke, *J. Chem. Phys.* **1993**, *98*, 5648–5652.
S10.   Gaussian 16, Revision C.01, M. J. Frisch, G. W. Trucks, H. B. Schlegel, G. E. Scuseria, M. A. Robb, J. R. Cheeseman, G. Scalmani, V. Barone, G. A. Petersson, H. Nakatsuji, X. Li, M. Caricato, A. V. Marenich, J. Bloino, B. G. Janesko, R. Gomperts, B. Mennucci, H. P. Hratchian, J. V. Ortiz, A. F. Izmaylov, J. L. Sonnenberg, D. Williams-Young, F. Ding, F. Lipparini, F. Egidi, J. Goings, B. Peng, A. Petrone, T. Henderson, D. Ranasinghe, V. G. Zakrzewski, J. Gao, N. Rega, G. Zheng, W. Liang, M. Hada, M. Ehara, K. Toyota, R. Fukuda, J. Hasegawa, M. Ishida, T. Nakajima, Y. Honda, O. Kitao, H. Nakai, T. Vreven, K. Throssell, J. A. Montgomery, Jr., J. E. Peralta, F. Ogliaro, M. J. Bearpark, J. J. Heyd, E. N. Brothers, K. N. Kudin, V. N. Staroverov, T. A. Keith, R. Kobayashi, J. Normand, K. Raghavachari, A. P. Rendell, J. C. Burant, S. S. Iyengar, J. Tomasi, M. Cossi, J. M. Millam, M. Klene, C. Adamo, R. Cammi, J. W. Ochterski, R. L. Martin, K. Morokuma, O. Farkas, J. B. Foresman, D. J. Fox, Gaussian, Inc., Wallingford CT, 2016.
S11.   P. J. Hay and W. R. Wadt, *J. Chem. Phys.*, 1985, **82**, 299–310.
S12.   P. C. Hariharan and J. A. Pople, *Theor. Chim. Acta*, 1973, **28**, 213–222.
S13.   M. E. Casida, C. Jamorski, K. C. Casida and D. R. Salahub, *J. Chem. Phys.*, 1998, **108**, 4439–4449.
S14.   R. E. Stratmann, G. E. Scuseria and M. J. Frisch, *J. Chem. Phys.*, 1998, **109**, 8218–8224.

Table S1. Crystallographic data and structure refinements for [PtRhCl$_2$(piam)$_2$(NH$_3$)$_2$(PPh$_3$)]$_2$[CuCl$_4$]·2MeCN (**2**).

	2
Empirical formula	C$_{60}$H$_{88}$Cl$_8$CuN$_{10}$O$_4$P$_2$Pt$_2$Rh$_2$
Formula weight	2018.48
Crystal system	Monoclinic
Space group	$P2_1/n$
a (Å)	12.3638(3)
b (Å)	23.3713(7)
c (Å)	13.5306(4)
α (°)	90
β (°)	108.696(3)
γ (°)	90
V (Å^3)	3703.47(19)
Z	2
Temperature (K)	123
Dc (Mgm^{-3})	1.810
Absorption coefficient (mm^{-1})	4.864
$F(000)$	1982
Crystal size (mm^3)	0.70 ×0.50 × 0.35
Measured reflections	28662
Independent reflections	8483 [R_{int} = 0.0197]
Data/restraints/parameters	8483/0/412
Goodness-of fit on F^2	0.807
R [$I > 2\sigma(I)$]	R_1 = 0.0211, wR_2 = 0.0898
R (all data)	R_1 = 0.0232, wR_2 = 0.0923

Table S2. Comparison of selected bond distances (Å).

Compounds	M–Pt	Pt–Rh	Rh–P
[PtRhCl$_3$(piam)$_2$(NH$_3$)$_2$]·4H$_2$O	-	2.5704(7)	-
1	-	2.7289(8)	2.273(2)
2	Cu---Pt = 3.14655(12)	2.7328(2)	2.2541(7)
3	Cu---Pt = 3.1632(11)	2.7197(5)	2.2515(16)
	Cu---Pt = 3.0472(9)	2.7092(5)	2.2915(15)
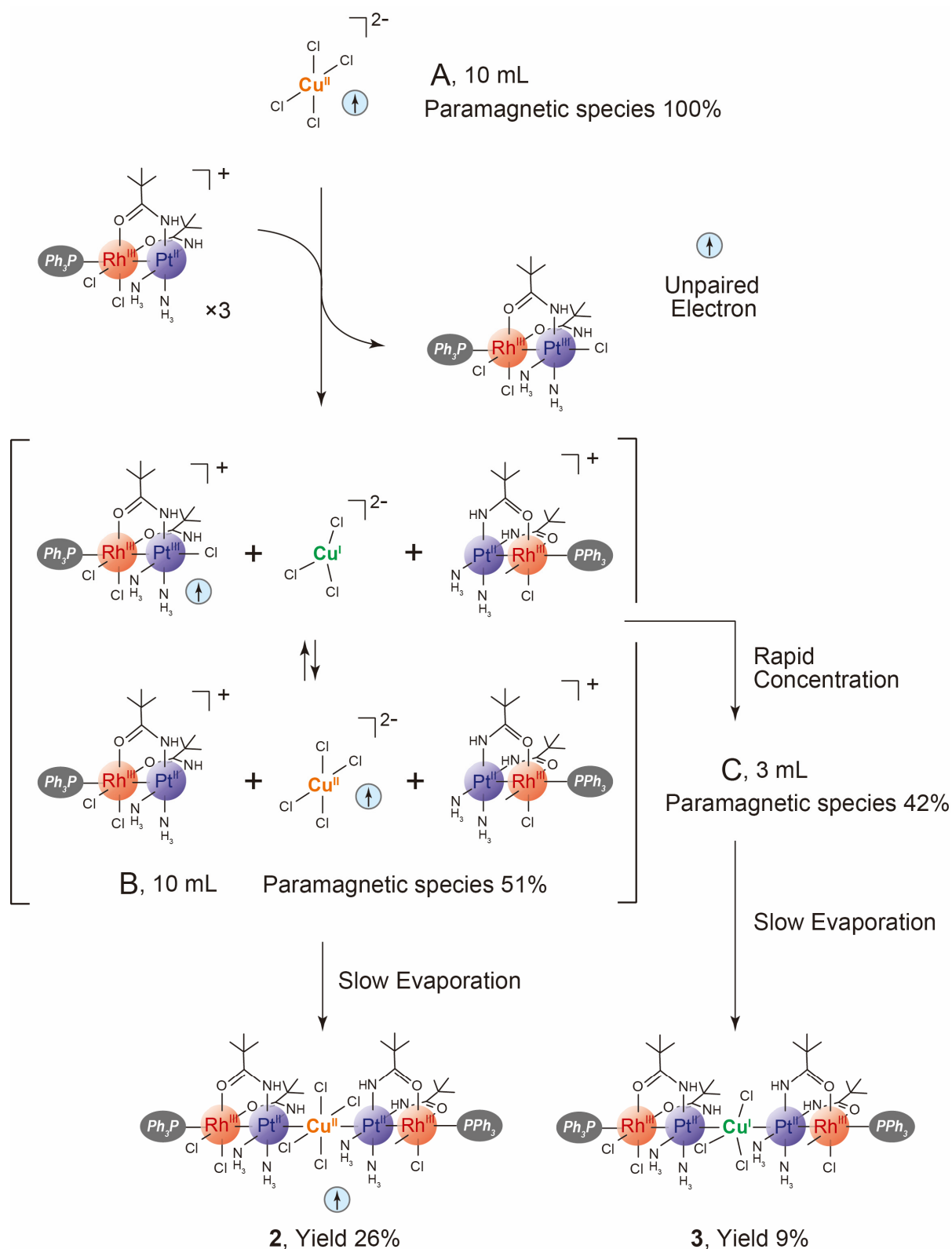
Scheme S1. Proposed experimental scheme for (Bu₄N)₂[CuCl₄] (30 μmol) and [PtRhCl₂(piam)₂(NH₃)₂(PPh₃)]PF₆ (**1**, 90 μmol) in MeCN 10 mL. Detailed explanation is mentioned in the synthetic studies for isolation of [PtRhCl₂(piam)₂(NH₃)₂(PPh₃)]₂[CuCl₄]·2MeCN (**2**).
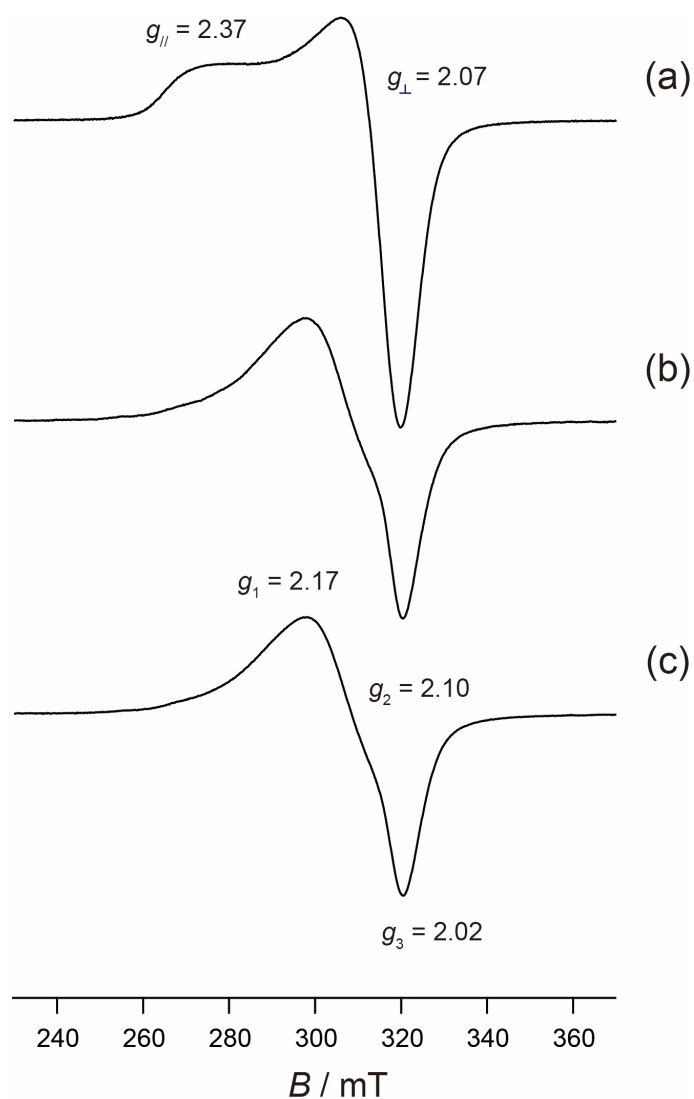
Figure S1. Continuous wave EPR spectra of glasses (a) A, (b) B, and (c) C at 77 K. The volume 0.1 mL of each sample was measured, and the area ratios were converted by the corresponding volume. Experimental settings: microwave frequency, (a) 9.057, (b) 9.059, and (c) 9.059 GHz; microwave power, 6 mW; field modulation, 0.2 mT.
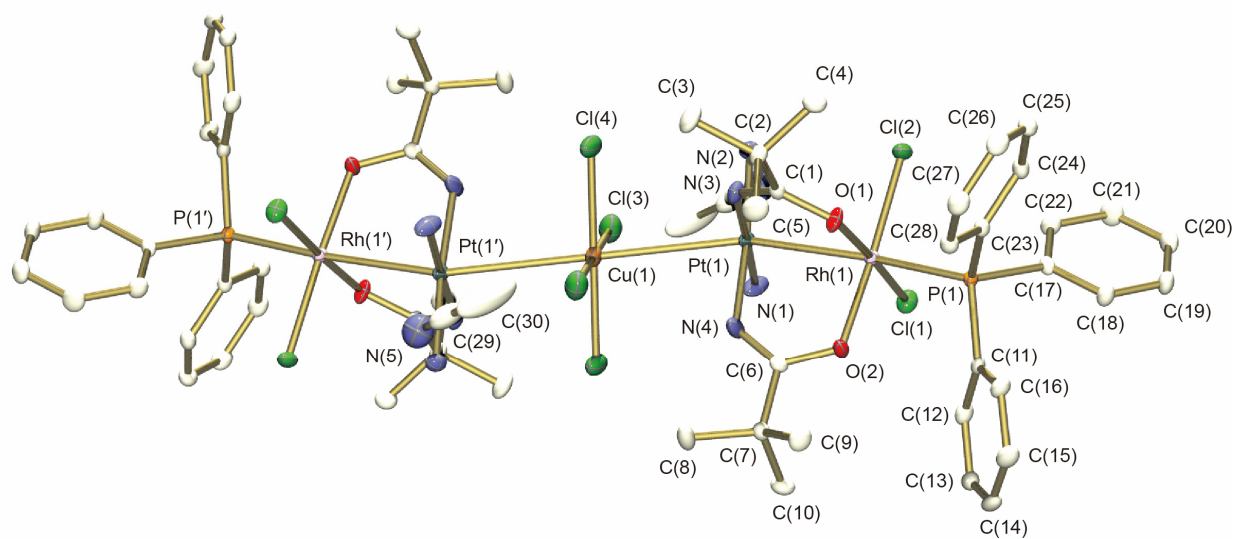
Figure S2. Crystal structure of $[PtRhCl_2(piam)_2(NH_3)_2(PPh_3)]_2[CuCl_4] \cdot 2MeCN$ (**2**). Hydrogen atoms are omitted for clarity.
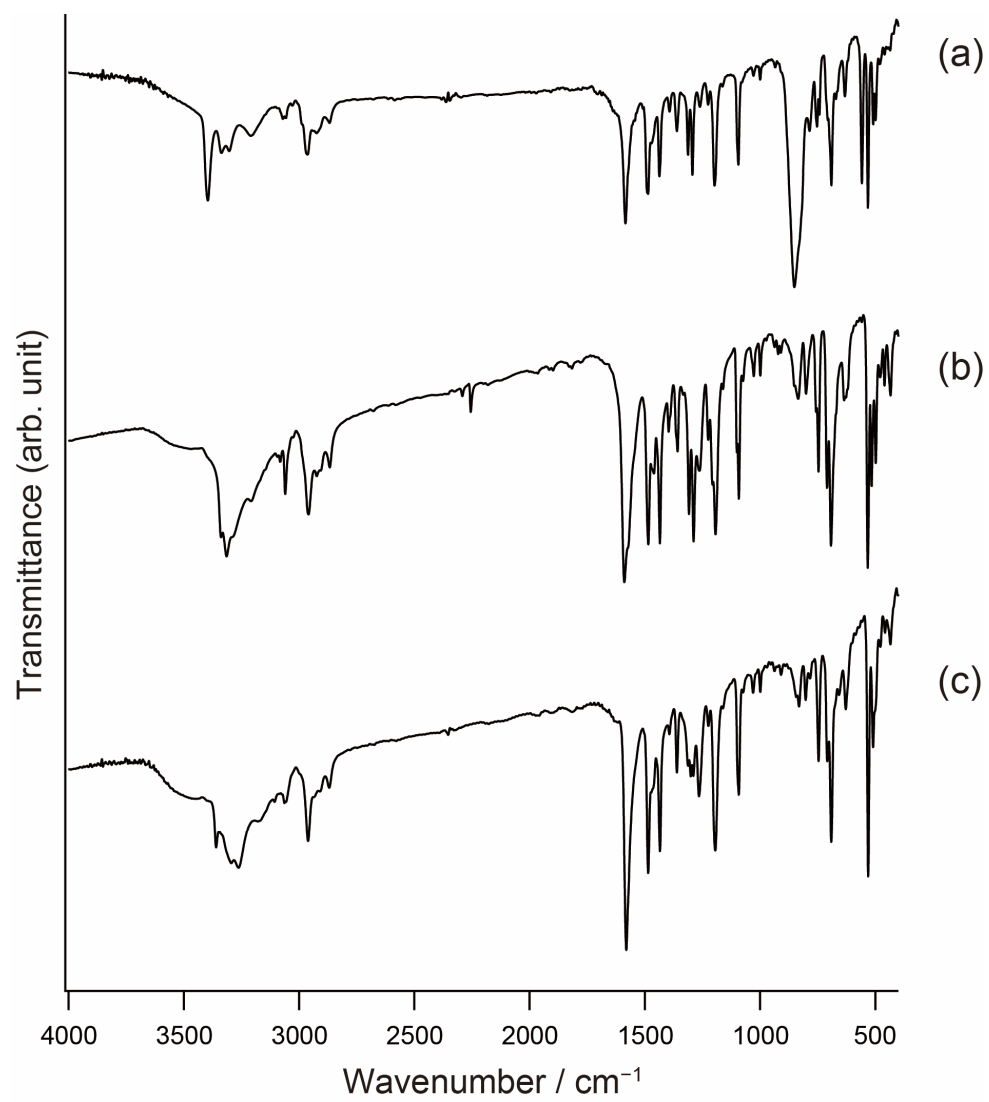
Figure S3. IR spectra (KBr pellet) of (a) **1**, (b) **2**, and (b) **3**.
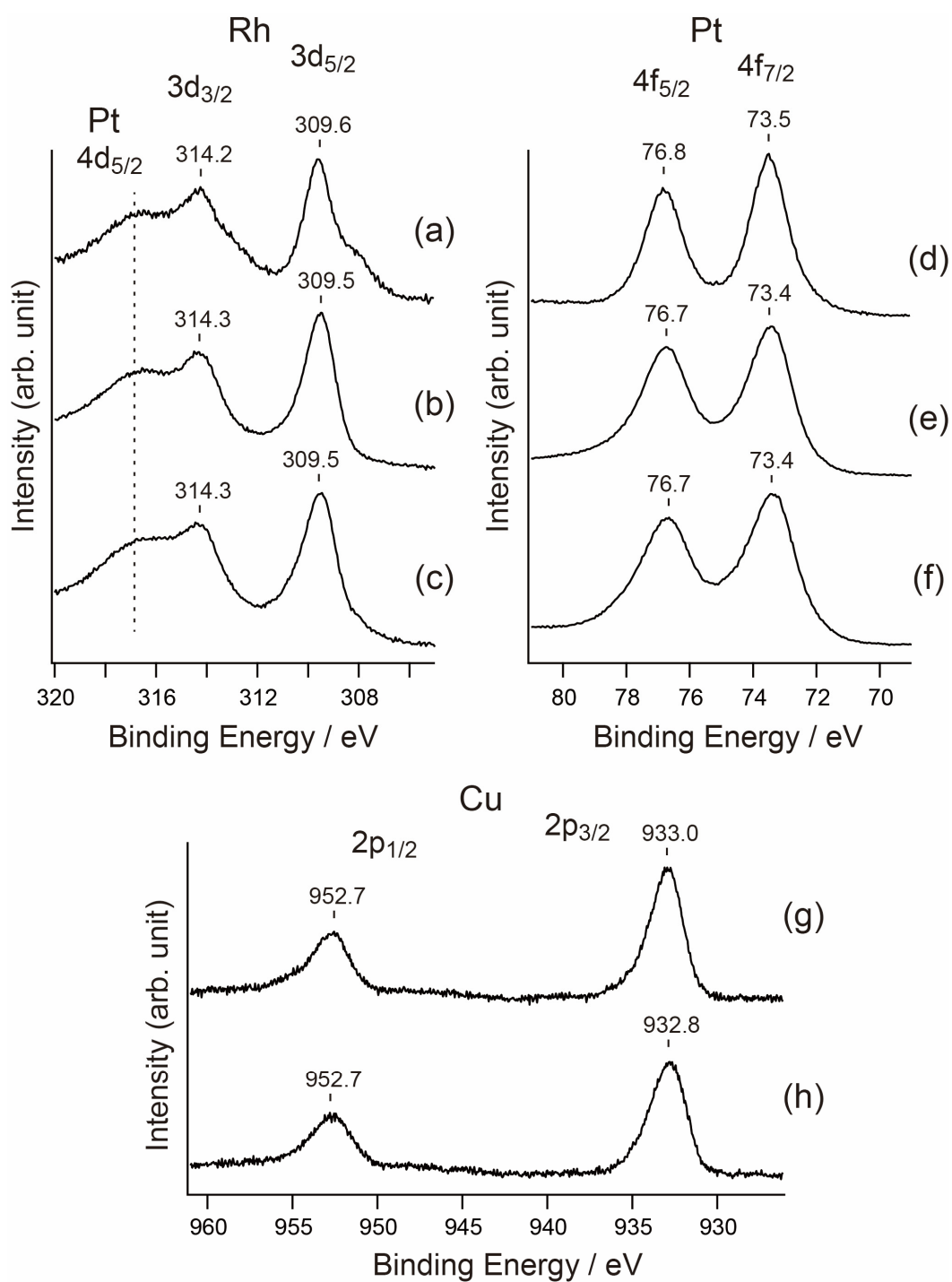
Figure S4. Rh $3d_{3/2}$ and $3d_{5/2}$ core levels of XPS for (a) **1**, (b) **2**, and (c) **3**. Pt $4f_{5/2}$ and $4f_{7/2}$ core levels of XPS for (d) **1**, (e) **2**, and (f) **3**. Cu $2p_{1/2}$ and $2p_{3/2}$ core levels of XPS for (g) **2** and (h) **3**.
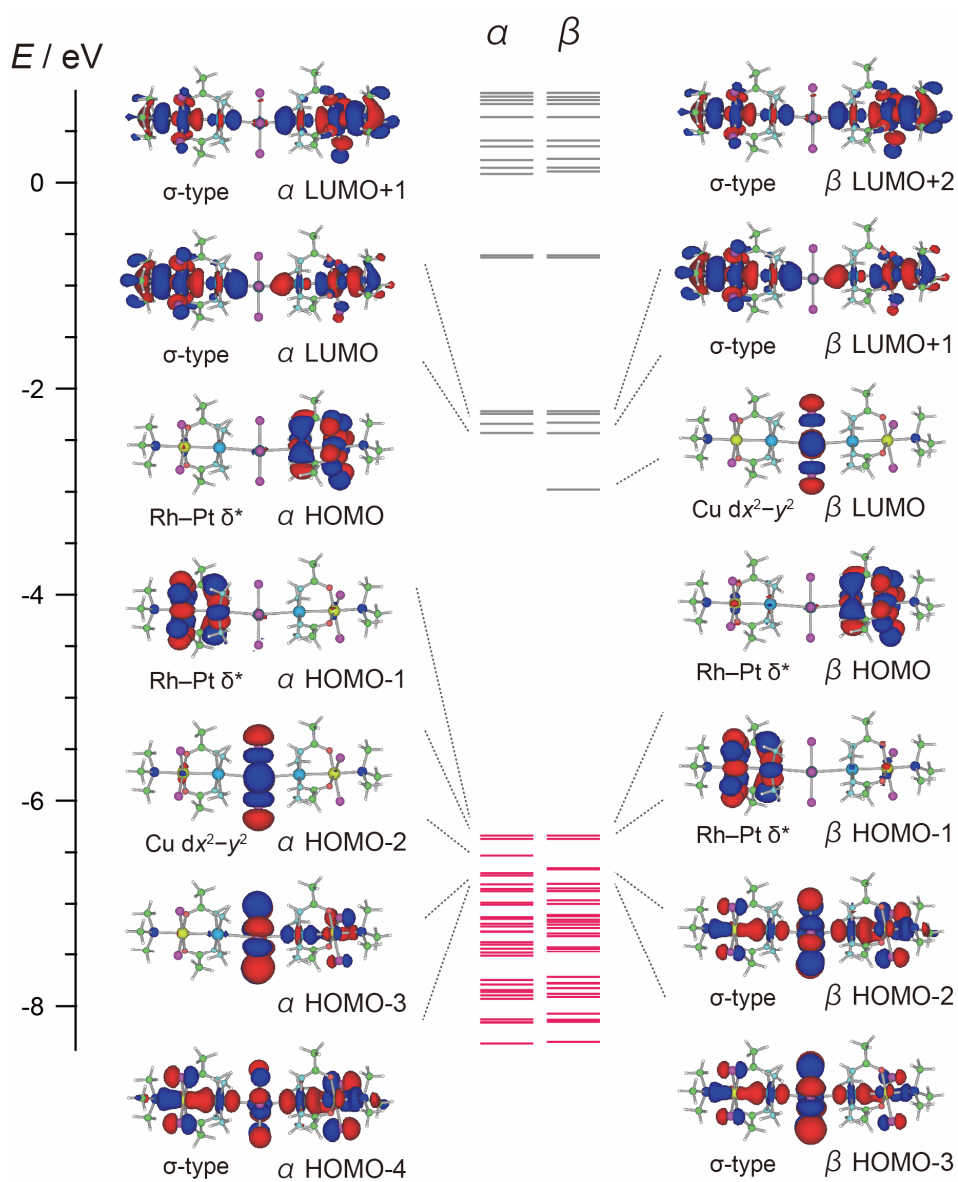
Figure S5. Energy diagrams with selected molecular orbitals for [PtRhCl$_2$(NHCOCH$_3$)$_2$(NH$_3$)$_2$(PMe$_3$)]$_2$[CuCl$_4$] obtained by DFT calculation considering the solvation effect of MeCN.

α LUMO+6

α LUMO

α HOMO-5

α LUMO+5

α HOMO

α HOMO-6

α LUMO+4

α HOMO-1

α HOMO-7

α LUMO+3

α HOMO-2

α HOMO-8

α LUMO+2

α HOMO-3

α HOMO-9

α LUMO+1

α HOMO-4

α HOMO-10

β LUMO+6

β LUMO

β HOMO-5

β LUMO+5

β HOMO

β HOMO-6

β LUMO+4

β HOMO-1

β HOMO-7

β LUMO+3

β HOMO-2

β HOMO-8

β LUMO+2

β HOMO-3

β HOMO-9

β LUMO+1
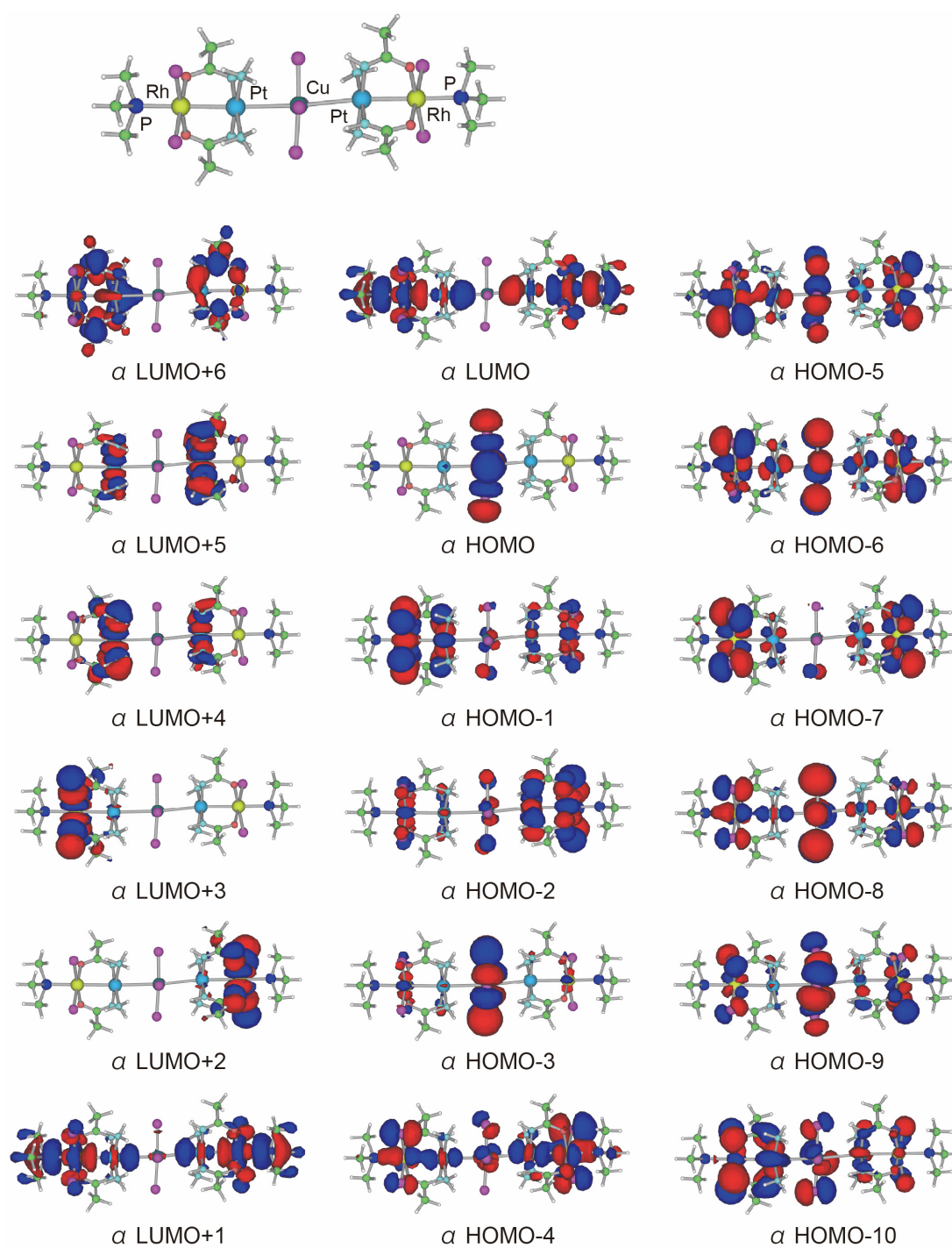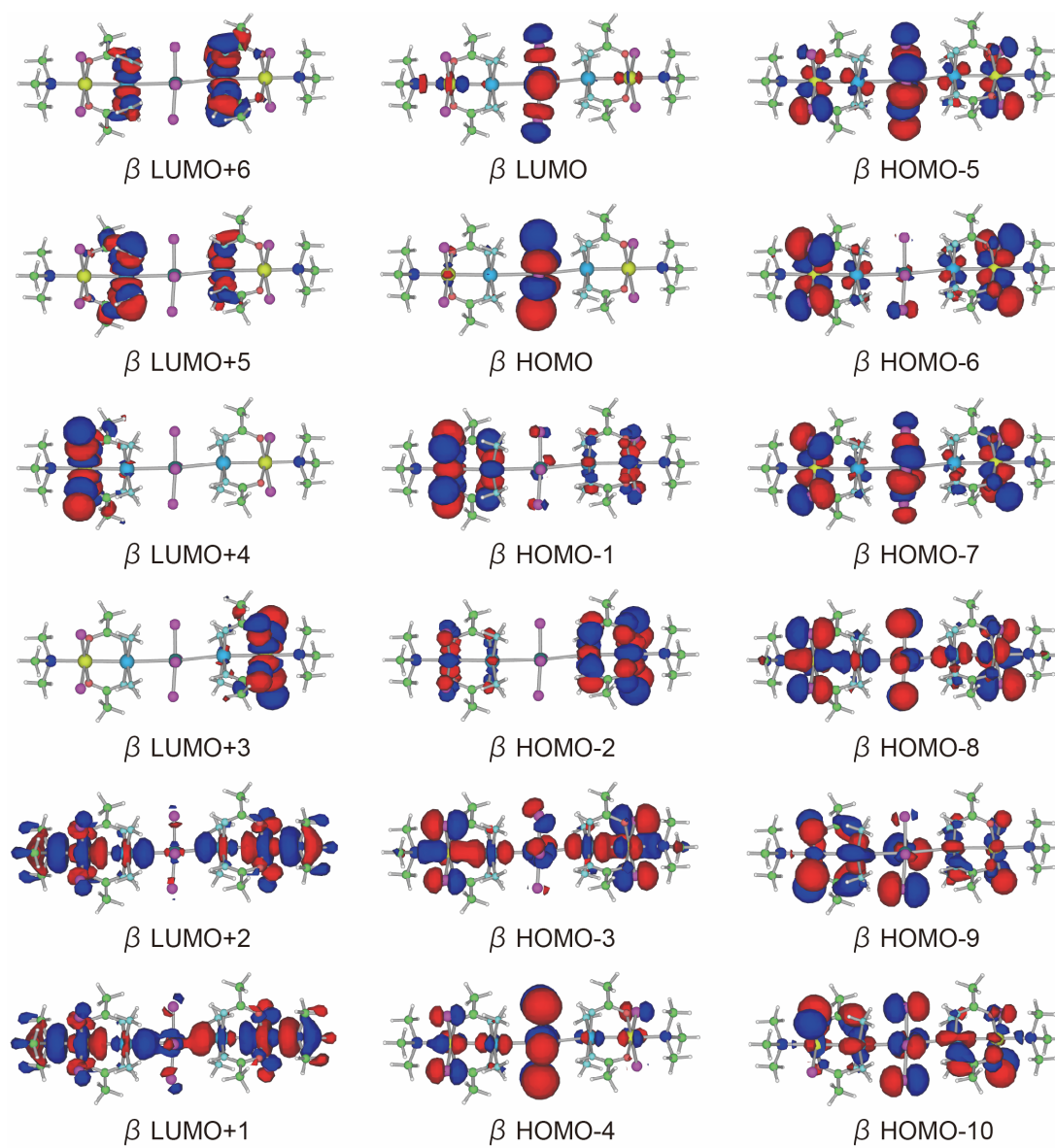
β HOMO-4

β HOMO-10

Figure S6. Result of DFT calculation of [{PtRhCl$_2$(NHCOCH$_3$)$_2$(NH$_3$)$_2$(PMe$_3$)}$_2${CuCl$_4$}] performed under vacuum condition.
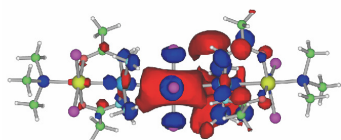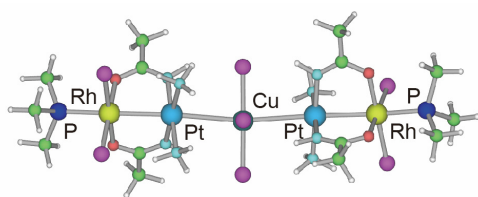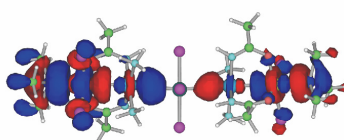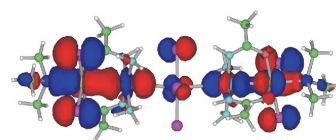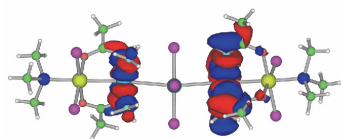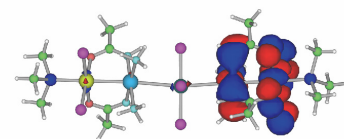
α LUMO+6

α LUMO

α HOMO-5

α LUMO+5

α HOMO

α HOMO-6

α LUMO+4

α HOMO-1

α HOMO-7

α LUMO+3

α HOMO-2

α HOMO-8

α LUMO+2

α HOMO-3

α HOMO-9

α LUMO+1

α HOMO-4

α HOMO-10

β LUMO+6   β LUMO   β HOMO-5

β LUMO+5   β HOMO   β HOMO-6

β LUMO+4   β HOMO-1   β HOMO-7

β LUMO+3   β HOMO-2   β HOMO-8

β LUMO+2   β HOMO-3   β HOMO-9
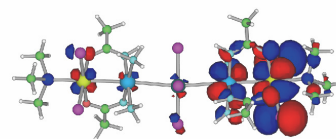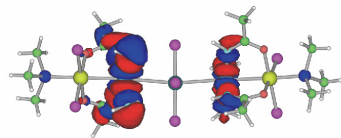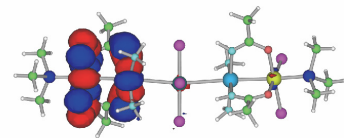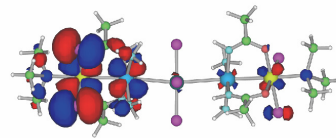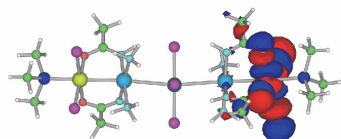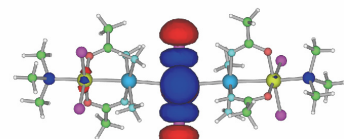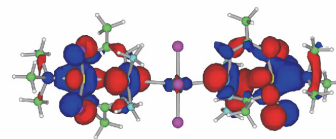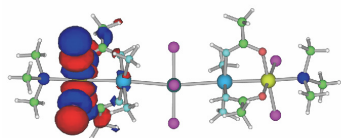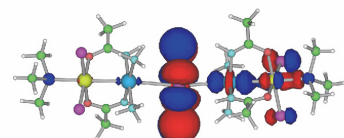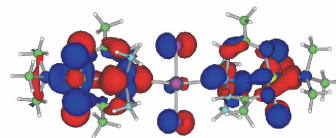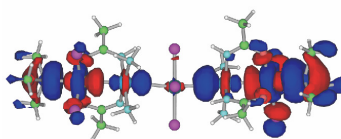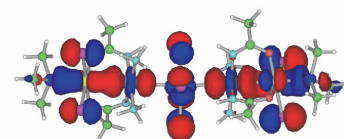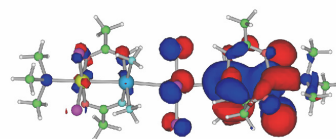
β LUMO+1   β HOMO-4   β HOMO-10
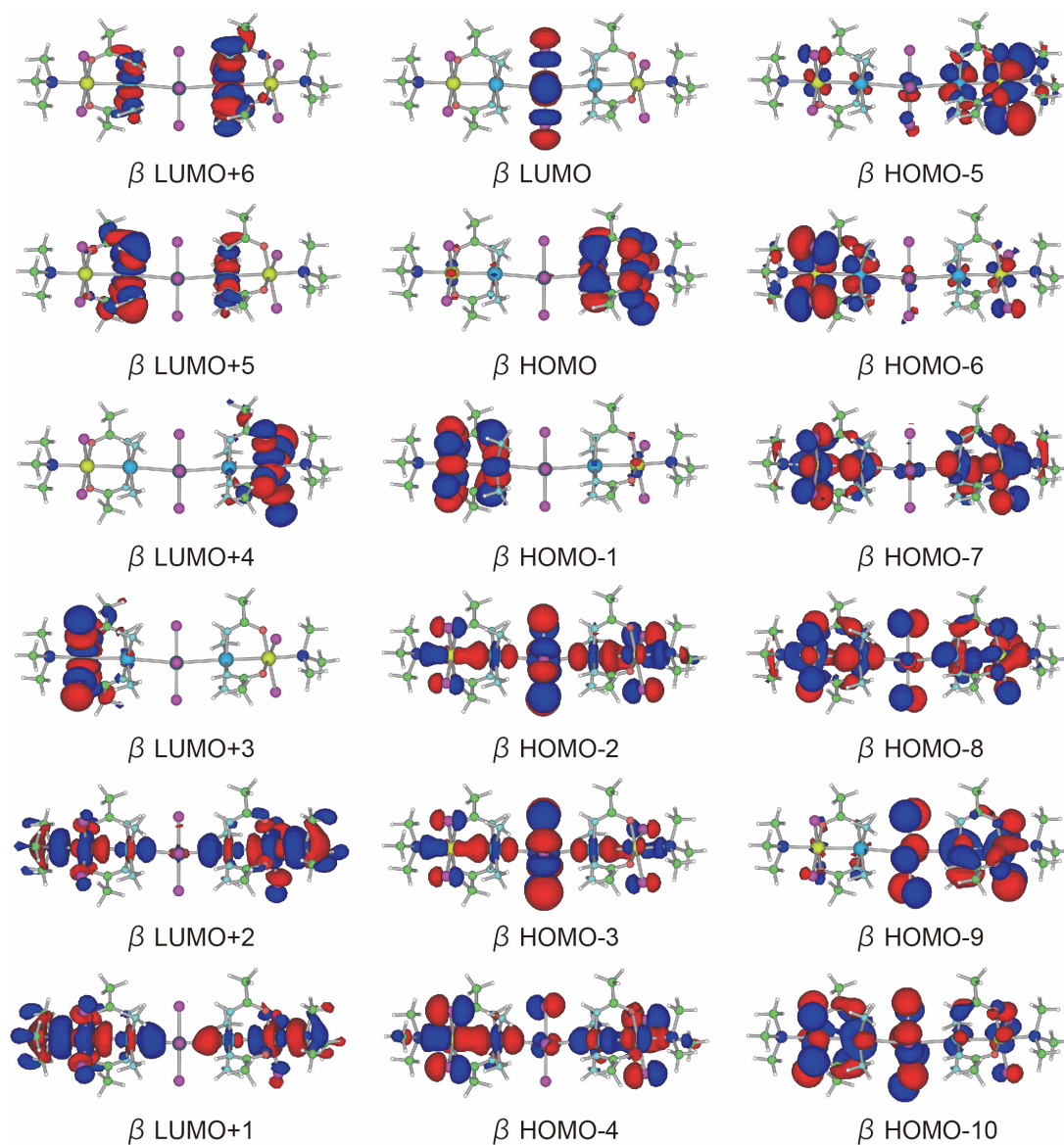
Figure S7. Result of DFT calculation of $[\{PtRhCl_2(NHCOCH_3)_2(NH_3)_2(PMe_3)\}_2\{CuCl_4\}]$ considering solvation effect of MeCN.
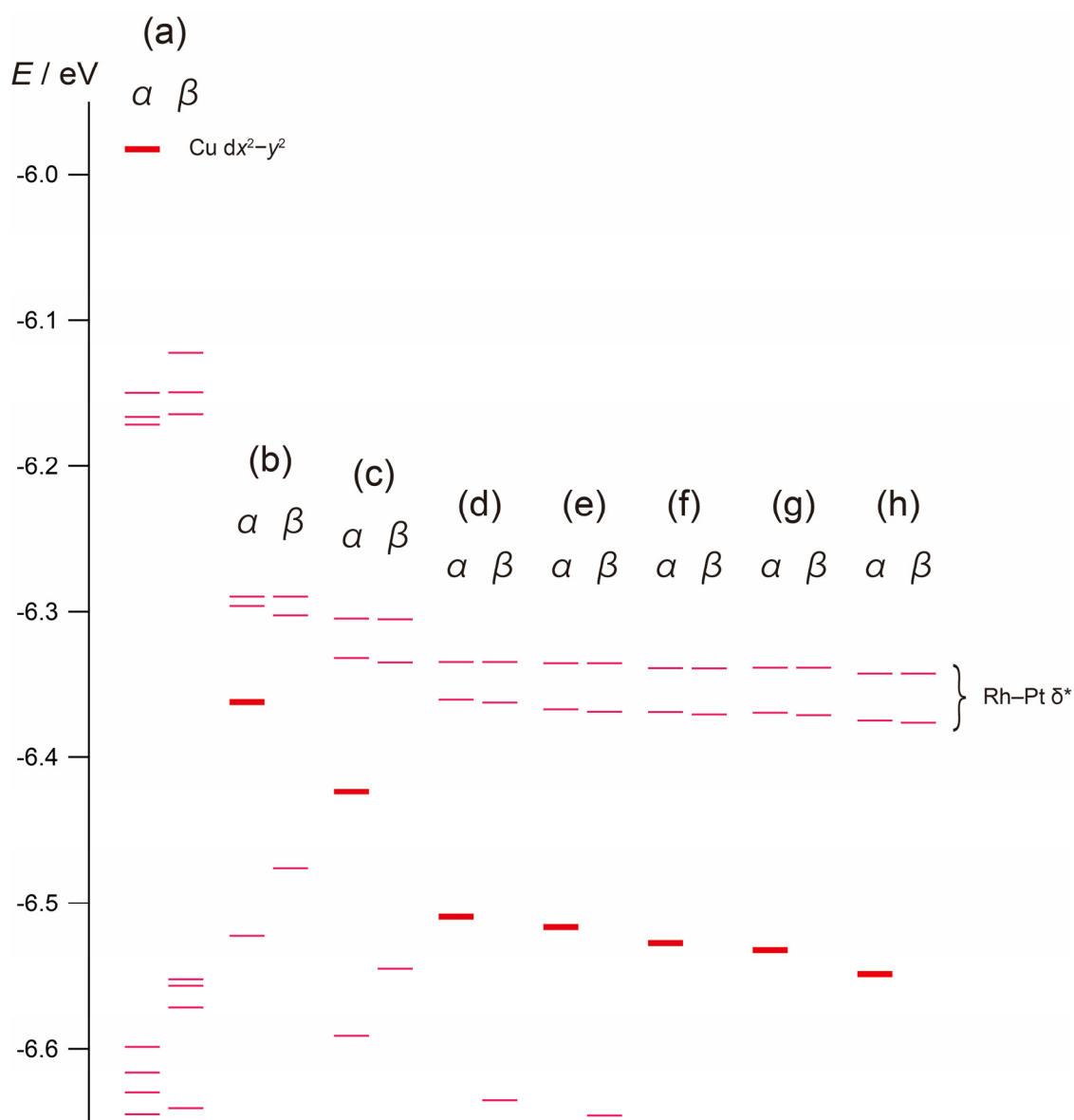
Figure S8. Energy diagrams around HOMO for [PtRhCl$_2$(NHCOCH$_3$)$_2$(NH$_3$)$_2$(PMe$_3$)]$_2$[CuCl$_4$] obtained by DFT calculation (a) under the vacuum condition, considering the solvation effect of (b) CHCl$_3$, (c) THF, (d) Me$_2$CO, (e) EtOH, (f) MeOH, (g) MeCN, and (h) H$_2$O. Thick lines represent Cu dx^2-y^2 orbitals.
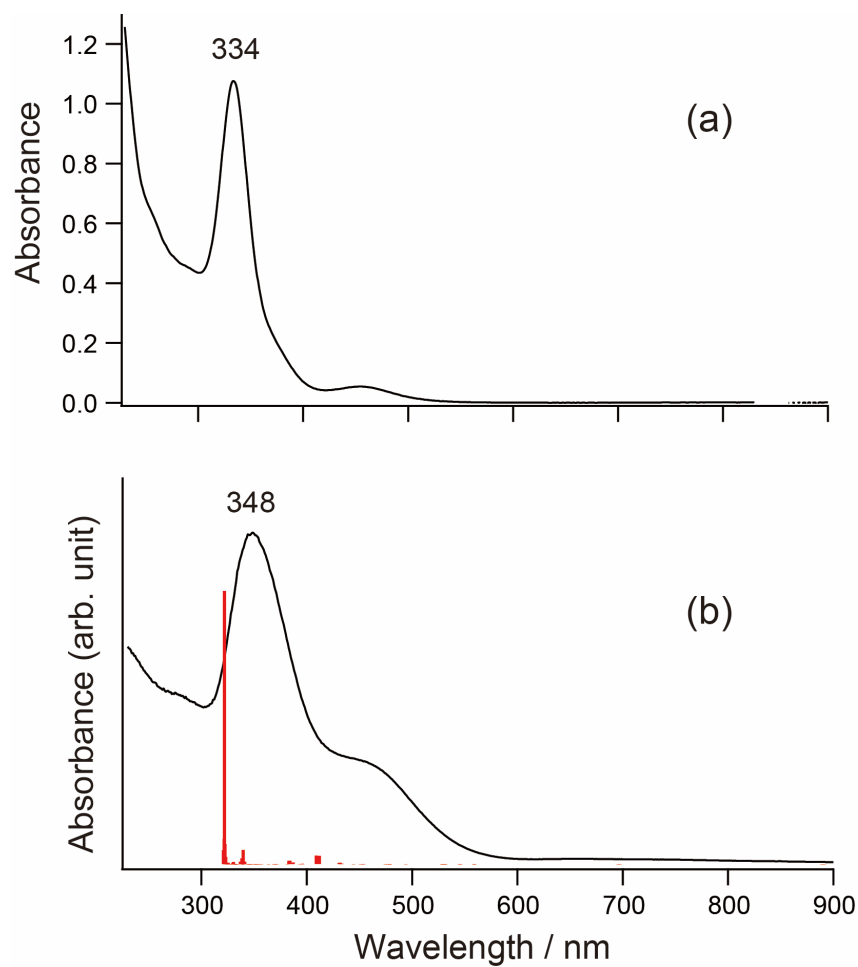
Figure S9. (a) UV–vis spectra of 0.025 mM MeCN solution containing **2** with optical path length l = 1.0 cm, and (b) diffuse reflectance spectra of **2**. Red bars are results of Td-DFT calculation. The bar at 321.7 nm (f = 0.4712) is α-HOMO−3 → LUMO+1 and β-HOMO−2 → LUMO+1, 339.5 nm (f = 0.0248) is β-HOMO → LUMO+1 and β-HOMO → LUMO+2, 409.0 nm (f = 0.0148) is β-HOMO−9 → LUMO, and 411.9 nm (f = 0.0144) is β-HOMO−10 → LUMO.
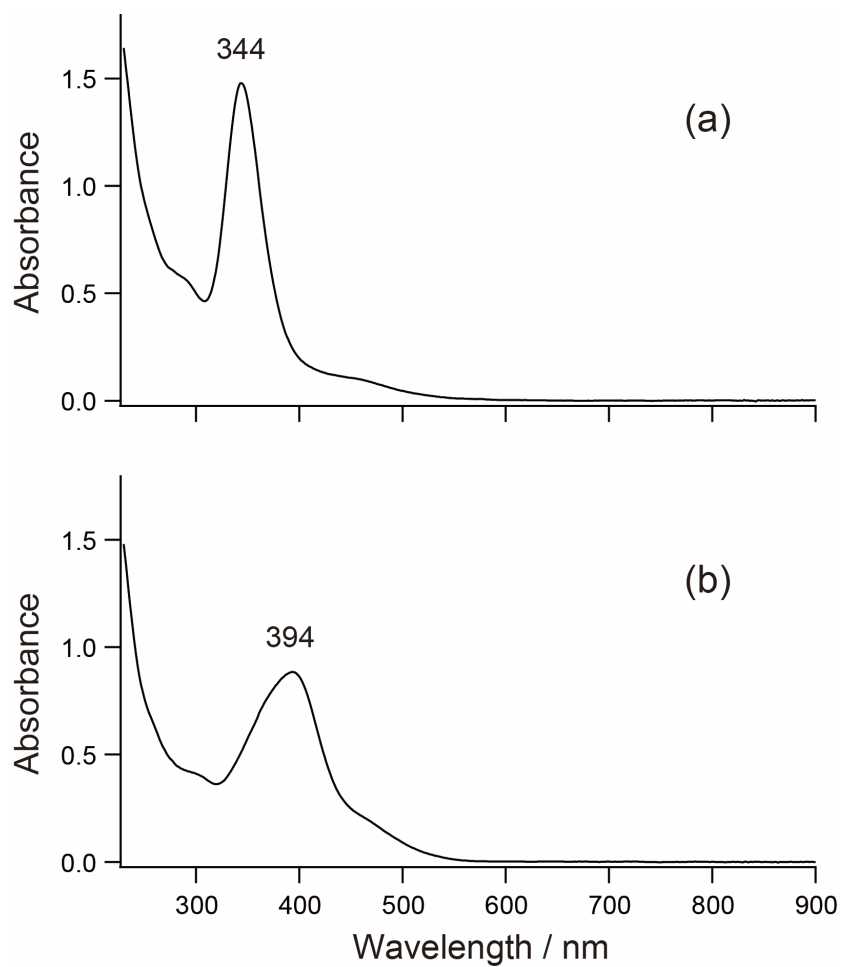
Figure S10. UV–vis spectra of 0.025 mM CH_2Cl_2 solution containing (a) **2** and (b) **3** with optical path length $l = 1.0$ cm.
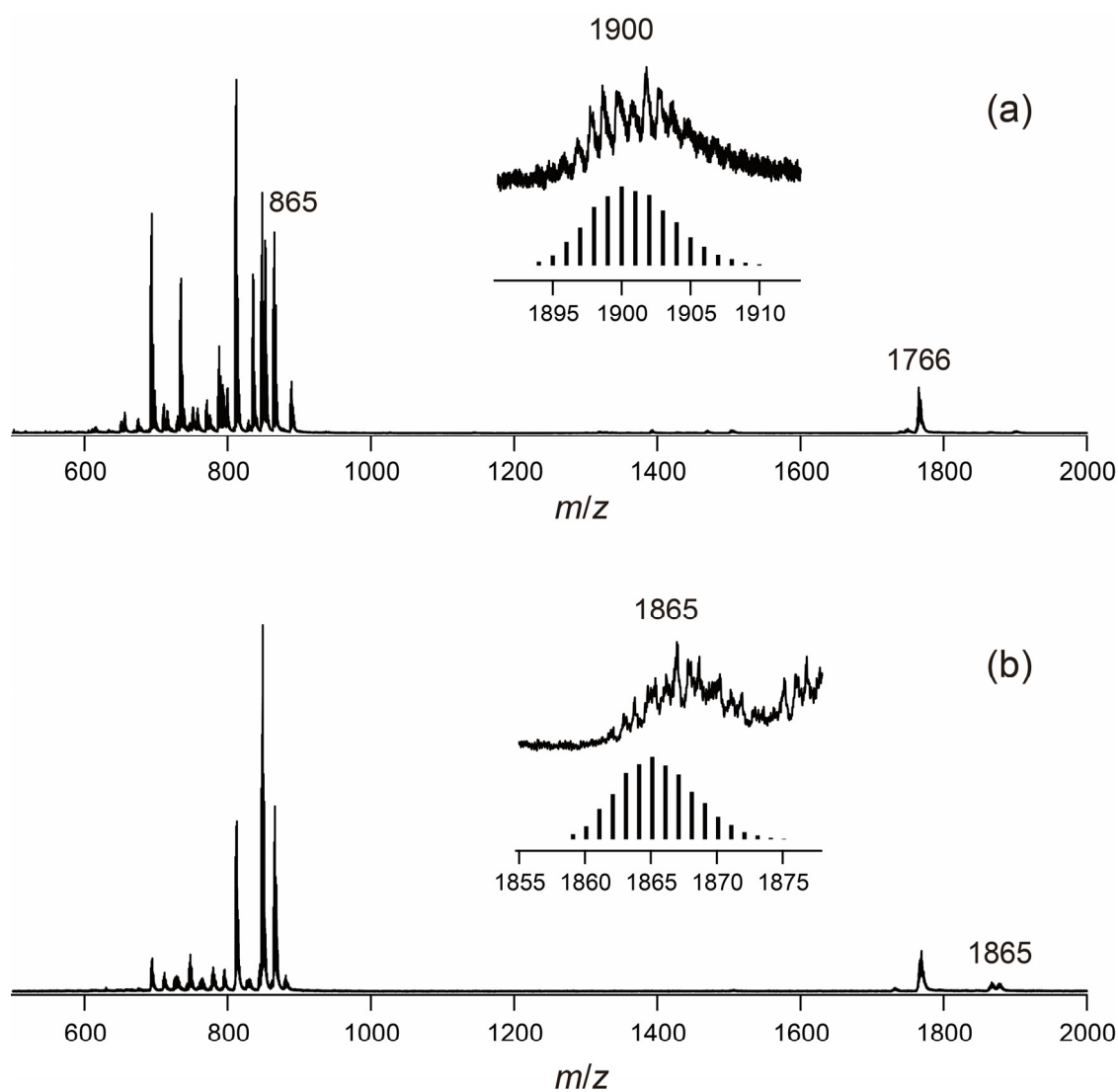
Figure S11. ESI-MS (positive) of (a) dilute MeCN solution containing **2** and (b) dilute MeOH solution containing **3**. The peaks at m/z = 1900 and 1865 are corresponding to $\{[PtRhCl_2(piam)_2(NH_3)_2(PPh_3)]_2[CuCl_3]\}^+$ and $\{[PtRhCl_2(piam)_2(NH_3)_2(PPh_3)]_2[CuCl_2]\}^+$, respectively, which are shown with calculated isotope patterns.
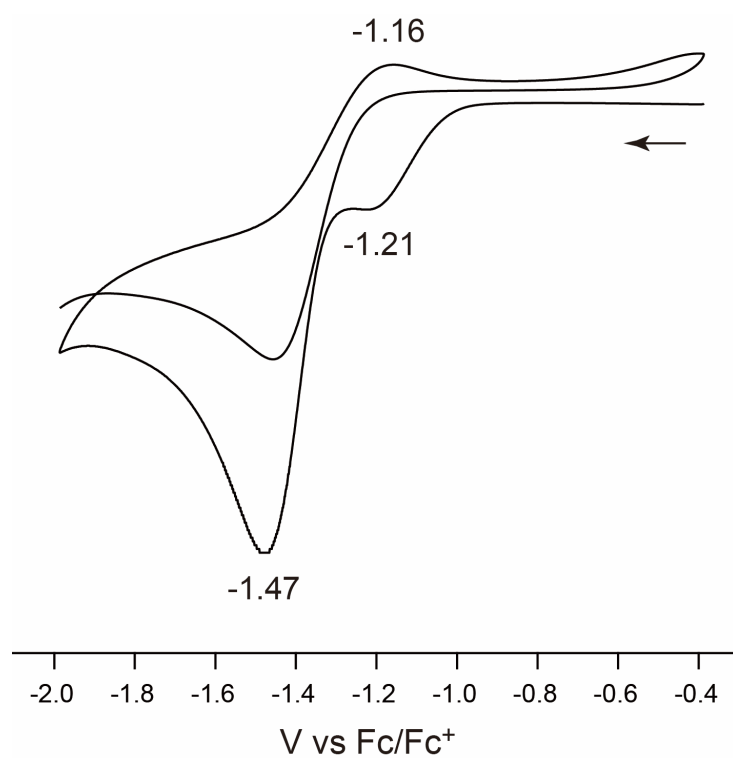
Figure S12. Cyclic voltammograms of **2** in MeCN in the presence of 0.1 M Bu₄NPF₆ as supporting electrolyte (scan rate 100 mV s^{-1}). The values are given with regard to Fc/Fc$^+$, which has been used as internal standard for calibration of the SCE reference electrode.